Finite-displacement Boltzmann transport theory reveals the detrimental effects of high-frequency normal modes on mobility

Zachary J. Knepp and Lisa A. Fredin [*]

Department of Chemistry, Lehigh University, 6 E. Packer Avenue, Bethlehem, Pennsylvania 18015, USA

Lattice vibrations can greatly reduce the charge-carrier mobilities of organic semiconductors by introducing dynamic structural disorder. The low-frequency regime is expected to contribute the most to this disorder since these vibrational modes result in the largest structural distortions and electronic coupling changes in time. In this work, a finite-displacement Boltzmann transport theory (Δ-BTE) method is developed to evaluate vibration-induced mobility effects in periodic boundary conditions. Δ-BTE is tested on a model organic semiconductor crystal, i.e., tetracene, and it predicts that particular high-frequency ring-breathing modes significantly reduce its mobility through a transient carrier localization process, even when restricted to the zero-point vibrational energy level.

I. INTRODUCTION

Crystalline organic semiconductors are modular materials with numerous applications including light emitting diodes, field effect transistors, photovoltaics, and sensors [1–5]. In organic materials, molecules pack together in various polymorphs primarily through noncovalent van der Waals forces [6–9]. Because of this, their solid structures are highly susceptible to both static and dynamic disorder. While examples of the former include packing defects and broken symmetries, dynamic disorder arises from stochastic combinations of lattice phonons, i.e., the normal vibrational modes of the crystal. This disorder transiently alters the inter- and intramolecular interactions between or within the molecules of the crystal [6,10–13].

Combinations of experimental and theoretical evidence suggest that dynamic disorder largely limits the charge-carrier mobilities of organic semiconductors by reducing intermolecular electronic couplings and by inducing charge-carrier localization from several molecules (≈ 10) down to single monomers [14–26]. This effect leads to a necessary shift in the description of the transport mechanism from delocalized bandlike to localized hopping and back depending on the time-varying phonon populations. While band and hopping models are able to provide reasonable approximations for electron-phonon coupling in organic semiconductor materials individually [27–32], neither can completely describe the transport mechanism [21,33–35]. Because disorder-induced localization limits electrical conduction in these materials, hopping models are often used to predict trends in mobility. Constant relaxation time Boltzmann transport theory has been shown to predict accurate mobility trends of organic crystals with substantially less computational effort than hopping-based models [32]. While the limitations of hopping and band-based models are well understood, they continue to be used to screen and understand trends in related sets of crystals because they are widely available, are based on fundamental physics, and provide insight in terms of chemical intuition.

Some models have included dynamic disorder by examining the effect of some normal modes on coupling in a crystal [27–31]. Of all the possible vibrational modes for a given material, the low-frequency regime results in the largest structural distortions on average since these populate vibrational excited states beyond the zero-point energy level. Such large displacement intermolecular motions induce large electronic structure rearrangements. The low-frequency regime has been studied using combinations of transmission electron microscopy (TEM), molecular dynamics (MD), and density functional theory (DFT) on various crystalline organic semiconductors [15,17,22]. Low-frequency modes dominate the electron-phonon scattering rates limiting the charge-carrier mobility [30]. In particular, the lowest-frequency mode of typical herringbone organic crystals, i.e., a long axis asymmetric sliding motion, significantly reduces intermolecular electronic coupling and leads to frequent transient localization events [17,23].

Theoretical studies investigating the dynamic disorder of various organic crystals often neglect the majority of the high-frequency regime (>207 cm^{-1}) because these modes are not expected to significantly reduce charge-carrier mobility [17,23,31,36–38]. Because the high-frequency modes are generally restricted to the ground vibrational state ($n = 0$) at room temperature, according to the Bose-Einstein occupation number, they result in root-mean-square displacements (RMSDs) up to two orders of magnitude less than the low-frequency regime. However, inclusion of the full frequency range leads to more accurate mobilities [39,40] and shows that many modes contribute to dynamic disorder [39,41]. This is because electronic structure reorganization is not necessarily correlated with atomic displacement amplitudes.

In this study, the dynamic disorder of tetracene, a prototypical organic semiconductor crystal, is investigated to reveal the effects that each of its 180 Γ-point normal

[*]lafredin@lehigh.edu

TABLE I. Unit-cell lattice vectors and angles of the PBEsol0-3c optimized and the experimental triclinic TETCEN unit cell [42].

	a (Å)	b (Å)	c (Å)	α (deg)	β (deg)	γ (deg)	V (Å^3)
TETCEN	7.90	6.03	13.53	100.30	113.20	86.30	582.85
PBEsol0-3c	7.99	6.03	13.57	100.75	112.68	86.24	592.96

TABLE II. BTE-derived conductivity tensor matrix elements at the computed Fermi level of the PBEsol0-3c structure. Here, the carrier concentration is $\rho \equiv N_{\mathcal{F},T}/V$. The constant relaxation time τ is set to 2 fs.

	σ_{xx} (S/cm)	σ_{xy}	σ_{xz}	σ_{yy}	σ_{yz}	σ_{zz}	σ_1	σ_2	σ_3	ρ (cm^{-3})
PBEsol0-3c	43.5	−20.9	0.0	22.4	0.2	6.2	56.4	9.5	6.2	2.9×10^{20}

modes has on the anisotropic charge-carrier mobility. This is accomplished using a quantum-harmonic-oscillator-based finite-displacement Boltzmann transport theory model (Δ-BTE). Finite-displacement amplitudes are derived from the uncertainty in the position of each atom, which differs from the classical analog where displacements are set at the edge of the harmonic well [31]. A substantial benefit of Δ-BTE is that it does not require dimer extraction and electronic coupling evaluations, and thus serves as a high-throughput method for screening the normal-mode-induced mobility effects from band structure renormalization for a wide range of materials, including both inorganic (e.g., oxides, perovskites, metal organic frameworks) and organic (e.g., organic single crystals, covalent organic frameworks, interfaces).

II. COMPUTATIONAL METHODOLOGIES

The PBEsol0-3c solid-state composite density functional method was used to fully optimize the lattice parameters and nuclear coordinates of the tetracene (TETCEN) crystal structure [42] with the CRYSTAL17 code [43,44]. PBEsol0-3c combines a small atom-centered def2-mSVP basis set with geometric counterpoise corrections and Grimme's D3 dispersion corrections to accurately and affordably predict the geometric and electronic structure of many materials, including weakly bound organic semiconductor crystals [32,45,46]. For all calculations, the DIIS convergence accelerator was used. For the optimization, an anisotropic $4 \times 5 \times 3$ k-point mesh was generated via the shrinking factor (SHRINK) such that the real-space primitive lattice vectors multiplied by these were >30 Å. For the Boltzmann transport theory (BTE) calculations, the k-point mesh was quadrupled to increase the accuracy and to minimize the error of band derivatives. The self-consistent field (SCF) convergence threshold on total energy (TOLDEE) was set to 10^{-8} Hartree for the optimization and 10^{-10} Hartree for the frequency calculation. Tolerances for Coulomb and exchange sums (TOLINTEG) were set to 8 8 8 8 16 for all calculations.

III. RESULTS AND DISCUSSION

The density functional theory (DFT) optimized tetracene crystal structure closely matches the room-temperature TETCEN crystal structure with comparable lattice parameters and a primitive-cell volume that is only 1.73% larger than experiment (Table I) [42]. A Γ-point frequency calculation on the optimized structure produced only positive real eigenvalues, indicating a minimum. A band gap of 2.54 eV was predicted, which matches the experimental optical gap of 2.54 eV [47]. Due to a band crossing between the Γ-point and [−110] direction, the total theoretical bandwidth is the sum of the widths of the valence band edge (VB) and the VB-1 band. The predicted

valence bandwidth of 0.35 eV is comparable to previous DFT and experimental values of 0.39 eV [48] and 0.35–0.7 eV [49], respectively. The broad experimental range may be the result of vibrational effects or could be from the convolution of the bulk band structure with that of a reconstructed surface [48,49].

The fact that the geometric and the electronic structure of tetracene are well represented by the PBEsol0-3c composite density functional confirms its usefulness for predicting charge transport properties. The conductivity tensor [32] matrix elements in a Cartesian basis **x**, **y**, **z** within the constant relaxation time approximation of the Boltzmann transport equation (BTE, Appendix A) [30,43,44,50,51] can be derived from the optimized structure. By default, CRYSTAL17 aligns the **x** vector parallel to the optimized **a** lattice vector, then sets **y** 90° away and closest to the **b** axis, and then sets **z** orthogonal to **x** and **y** [43,44]. Because the BTE off-diagonal conductivity matrix elements are nonzero for tetracene, the tensor is diagonalized (Appendix B) to determine the principal axis eigenvectors and their corresponding eigenvalues (Table II).

According to BTE, tetracene preferentially conducts along the $\mathbf{e}_1$ direction (Fig. 1) at 56.4 S/cm when a constant relaxation time of 2 fs is assumed [52,53]. The angle between $\mathbf{e}_1$ and the **a** lattice vector ($\theta_{\mathbf{e}_1,a} = 148.4°$) agrees well with the experimental angle of 141.3° [22]. Substantially smaller conductivities are predicted in the $\mathbf{e}_2$ (9.5 S/cm) and $\mathbf{e}_3$ (6.2 S/cm) directions. In the $\mathbf{e}_1$ direction, the mobility is 1.2 cm^2/Vs
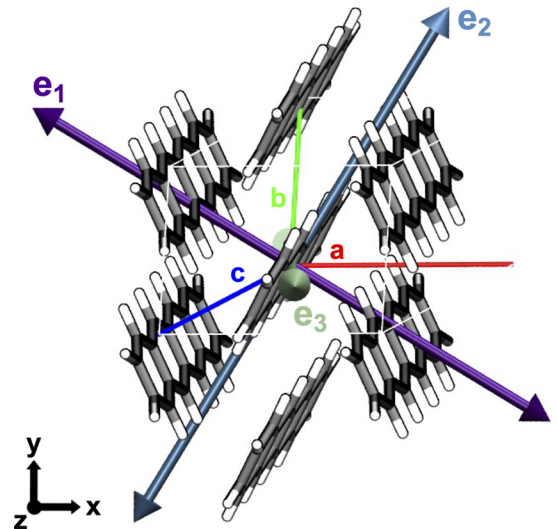

FIG. 1. Principal axis eigenvectors ($\mathbf{e}_1$, $\mathbf{e}_2$, $\mathbf{e}_3$) and the primitive lattice vectors (**a**, **b**, **c**) of the fully optimized PBEsol0-3c tetracene crystal structure.

TABLE III. BTE and experimental charge-carrier mobilities along the principal axes of the crystal.

	μ_1 (cm^2/Vs)	μ_2 (cm^2/Vs)	μ_3 (cm^2/Vs)	μ_1/μ_2	$\theta_{\mathbf{e}_1,a}$ (deg)
Experiment	$\mu_H = 0.8$ [22], 2.4 [54]	$\mu_L = 0.4$ [22]	–	$\mu_H/\mu_L \approx 1.5 - 2.0$ [22]	≈ 141.3 [22]
PBEsol0-3c	1.2	0.2	0.1	6.0	148.4

(Table III) when using the intrinsic carrier concentration from the number of carriers at the Fermi level divided by the primitive cell volume (Table II), which agrees well with experimental reports of 0.8 and 2.4 cm^2/Vs [22,54].

Projecting the principal axes mobilities in the high mobility plane (**ab**) produces a curve (Fig. 2) that agrees with experimental results for crystalline tetracene [22]. BTE predicts an anisotropy ratio between the high and low mobilities (μ_H/μ_L) of 6 in the high mobility plane, which is of the same order of magnitude as the experimental value of $\mu_H/\mu_L = 1.5–2$. Previous theoretical ratios predicted larger anisotropy ratios, i.e., >10 [55,56], indicating an improvement in the description of the electronic structure with PBEsol0-3c.

Δ-BTE quantifies the vibration-induced mobility change by calculating conductivity and carrier concentration at the Fermi level of the optimized and finite-displaced structures. The temperature-dependent finite-displacement amplitudes of each normal mode were determined from the DFT-derived uncertainty in the positions Eq. (C1). The approximation of finite displacements provides a way to correct for vibrational energy without relying on the electronic structure being linearly correlated to the vibration. Overall, the majority of the normal modes are harmonic in energy, with $R^2(0 \text{ K}) = 0.9940$ and $R^2(300 \text{ K}) = 0.9888$. A few of the high-frequency modes that do not significantly change the mobility are marginally anharmonic in energy (Fig. 3), even though their displacement amplitudes are harmonic.

The ground-state DFT bandwidth of 349 meV, approximated by the sum of the VB-1 and VB bandwidths because these bands cross, is within the 350–700 meV range of experimentally measured bandwidths [49]. As expected, the vibrationally perturbed (colored and gray) VB and VB-1 bands are significantly different in both energy and shape than the bands of the optimized structure (Fig. 4). Isolated normal modes and the averages over all the modes result in the narrowing of each band including the VB−1, VB, and VB+1 (Table IV). This is consistent with a band velocity reduction and a decrease in the charge-carrier mobility. Additionally, a sub-meV reduction in the bandwidths is observed as a function of increasing the temperature from 0 to 300 K.

TABLE IV. Widths of the frontier bands in meV, including the highest filled valence band (VB) and one band above (VB+1) and below (VB−1). The 0 and 300 K bandwidths are averaged over all the normal modes in both the negative and positive displacement directions.

	VB−1 (meV)	VB (meV)	VB+1 (meV)
PBEsol0-3c (opt)	161.1	188.1	270.5
PBEsol0-3c (0 K)	160.5	186.6	269.6
PBEsol0-3c (300 K)	160.4	186.2	269.3

Focusing in on normal mode # 4 (yellow), it is easy to see the effect of bandwidth narrowing as a function of populating higher vibrational excited states at 300 K when compared to the zero-point vibrational energy at 0 K. However, substantially larger bandwidth narrowing effects have been observed both experimentally and theoretically for oligoacene crystals from a combination of polaron formation and thermal lattice expansion, which Δ-BTE does not explicitly capture [55,57–60].

Normal-mode-induced mobility changes happen primarily in the $\mathbf{e}_1$ direction and very little in the $\mathbf{e}_2$ and $\mathbf{e}_3$ directions (Fig. 5). For each normal mode, the conductivity tensors were calculated and diagonalized at each of the normal-mode-perturbed Fermi levels. Calculated mobilities at 0 and 300 K (Fig. 6) show large changes across a wide range of frequencies. The percent change in mobility is reported as it results in the cancellation of τ, eliminating the constant relaxation but not the effects from electron-phonon scattering.

Interestingly, even though the majority of the modes are harmonic in energy, in either displacement direction, their resulting mobilities are not. This mobility anharmonicity is observed over the full frequency range at both 0 and 300 K. In fact, for particular modes in either the $+\mathbf{M}$ or $-\mathbf{M}$ direction, mobilities infrequently increased in magnitude, suggesting that those modes could be beneficial for charge transport. However, because each mode oscillates in both directions, the average mobility (Fig. 6, right) revealed that *all Γ-point normal modes are detrimental to the charge transport of tetracene* along the $\mathbf{e}_1$ direction.

Mobility differences between 0 and 300 K occur within the low-frequency regime (< 207 cm^{-1}) because low-frequency modes populate vibrational excited states, i.e., $n > 0$, at 300 K (Fig. 7). Differences in the average mobility changes (Fig. 8) up to 10% were found for the lowest-frequency normal mode
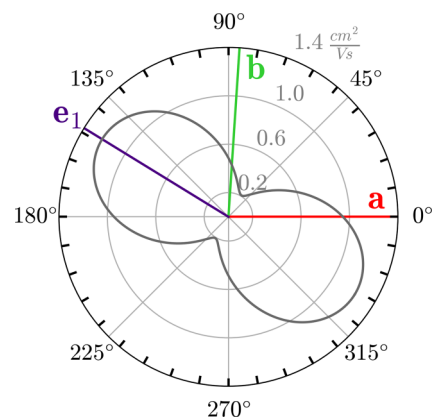

FIG. 2. Theoretically derived polar mobility curve in the **ab** plane of tetracene. The radial component corresponds to the counterclockwise degrees away from the a axis.
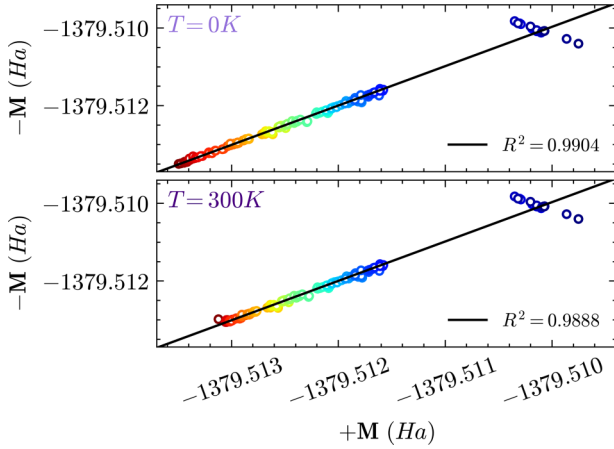
FIG. 3. Anharmonicity in the SCF displacement energies at 0 and 300 K due to the harmonic structural displacement of $+\mathbf{M}$ (x axis) and $-\mathbf{M}$ (y axis). The black line corresponds to the best-fit line between the positive and negative displacement energies.

FIG. 5. Normal-mode-induced mobility changes along the three primitive lattice directions ($\mathbf{e_1}$, $\mathbf{e_2}$, $\mathbf{e_3}$) averaged over the $+\mathbf{M}$ and $-\mathbf{M}$ finite displacements at 300 K.

at 300 K. As frequencies increase beyond 207 cm^{-1}, the differences between the two temperatures become negligible as the zero-point vibrational energy level is populated at all temperatures.

By inspecting the average mobility changes mode by mode, four normal modes were identified to significantly reduce the mobility (Figs. 6 and 9). Of the four, the second most
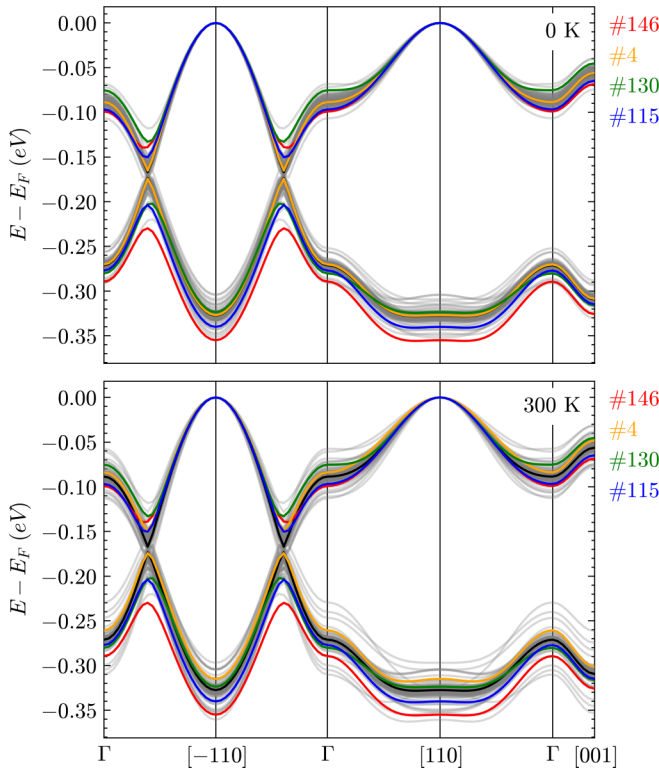

FIG. 4. Fully optimized (black) and the 0 K (top) and 300 K (bottom) finite-displaced (gray and colored) VB and VB-1 bands centered around the ground-state Fermi level. Particularly problematic modes (#) are highlighted in red, orange, green, and blue.
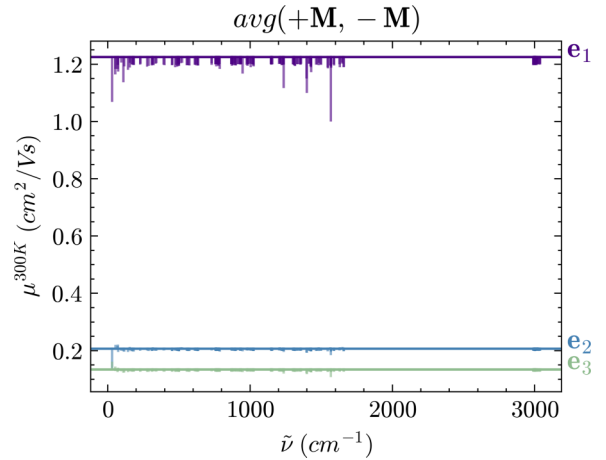
detrimental mode is the previously identified intermolecular asymmetric sliding motion [23]. Interestingly, particular high-frequency modes (modes 146, 130, and 115) lead to the first-, third-, and fourth-largest mobility reductions, up to 18.1%. Even though their average structural displacements are considerably small, of the order of 0.005–0.012 Å (Table V and Fig. 9), their detrimental impact on mobility is not (Table V). The effects of inelastic electron scattering from phonons likely limit the maximum mobility of tetracene significantly more than the band structure changes considered here, however it is still rather surprising that such small displacements lead to such large mobility changes. These findings are in contrast to previous assumptions that only large displacements have a large effect on the electronic structure. However, this parallels very recent insights that high-frequency modes contribute to dynamic disorder found using an electronic coupling-based approach [41].

To rationalize why these particular high-frequency modes are so problematic, the valence band projected density matrices are plotted as isosurfaces (Fig. 10). The *most* detrimental mode (mode 146, 1568 cm^{-1}) is characteristic of ring breathing and C-C-H in-plane bending. When compared to the fully optimized projected valence band, the motion (RMSD = 0.005 Å) results in a transiently localized polaronlike band density. Interestingly, as a function of the vibration, the density seemingly "hops" between the tetracene monomers along the principal $\mathbf{e_1}$ direction. It should be noted that this is a report of a *switch* in the charge transport mechanism between band and hopping by combining finite displacements with BTE. Until now, calculating such processes has required higher-level fragment orbital-based surface hopping methods [25].

Similar polaronic behavior is observed for the third (1398 cm^{-1}, ring breathing/C-C-H bending, RMSD = 0.005 Å) and fourth (1236 cm^{-1}, C-C-H bending, RMSD = 0.012 Å) modes, although to a lesser extent (Fig. 10). The intermolecular asymmetric sliding phonon (30 cm^{-1}, RMSD = 0.132 Å), however, does not appear to be polaronic. Instead, the asymmetric sliding motion leads to unfavorable orbital
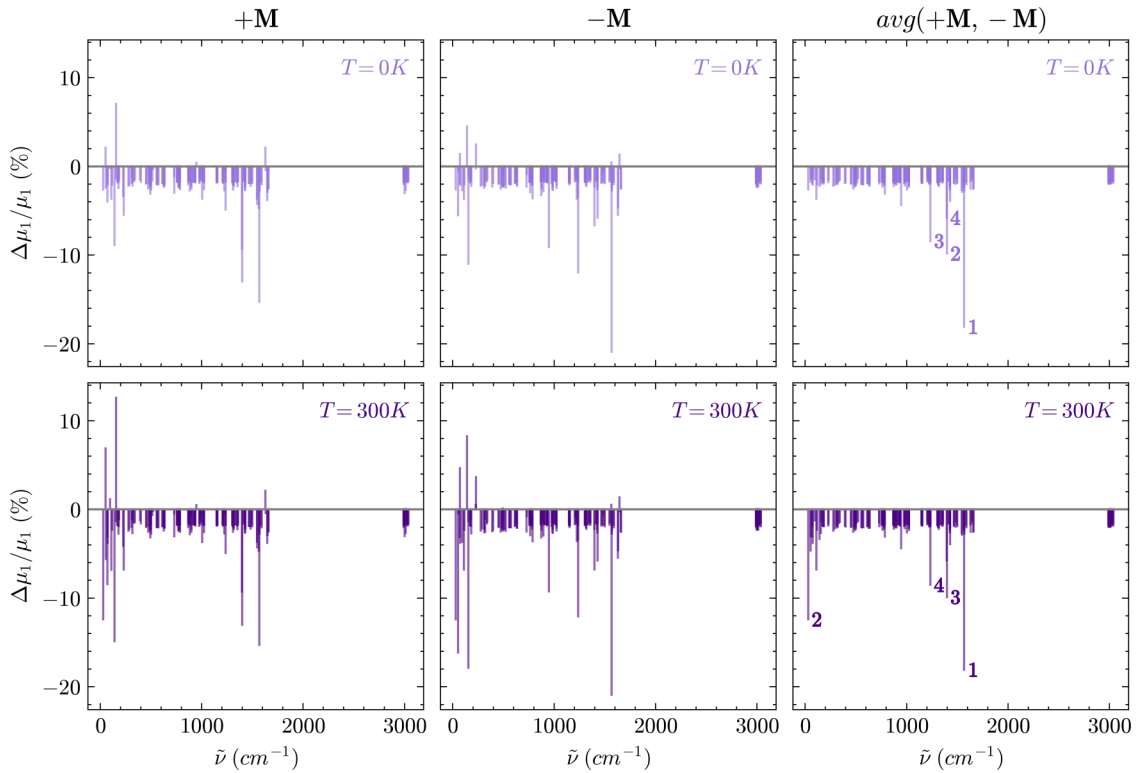
FIG. 6. Normal-mode-induced mobility changes along the principal axis (e_1) at 0 K (light purple, top) and 300 K (dark purple, bottom). $\Delta\mu/\mu$ is expressed as a percentage to allow for easy visualization along a single set of axes.

overlap and electronic coupling along the vibration, as reported previously [23,31]. Interestingly, according to BTE, it appears that the sliding phonon is detrimental in both directions of the oscillation, which differs from our results when evaluating pentacene with a Marcus dimer projection method [31].

to be identified. Surprisingly, three of tetracene's four most detrimental modes are high-frequency ring-breathing modes that appear to be polaronic. This means that neglecting the high-frequency regime when evaluating vibrational effects in molecular semiconductors misses an important part of the transport picture at finite temperatures.

IV. CONCLUSION

Δ-BTE is an efficient method for evaluating the dynamic disorder of molecular crystals with finite temperature and zero-point energy effects. It correctly predicts both the mobility magnitudes and the preferential transport direction of tetracene after conductivity tensor diagonalization. Δ-BTE is relatively cheap so the full frequency range can be explored. This allows high-frequency modes that result in significant mobility reductions, even with minuscule structural changes,

TABLE V. The four most detrimental modes identified by Δ-BTE at 0 and 300 K. The RMSDs were calculated on four molecule clusters extracted from the unit cells.

| Temperature (K)	Rank	mode (#)	RMSD (Å)	cm^{-1}	$\Delta\mu_1$ (cm^2/Vs)	$\Delta\mu_1/\mu_1$ (%)	Description
0	1	146	0.005	1568	−0.22	−18.1	ring breathing/C-C-H bending
	2	130	0.005	1398	−0.12	−9.8	ring breathing/C-C-H bending
	3	115	0.012	1236	−0.10	−8.4	C-C-H bending
	4	129	0.005	1397	−0.07	−5.8	C-C-H bending
300	1	146	0.005	1568	−0.22	−18.1	ring breathing/C-C-H bending
	2	4	0.132	30	−0.15	−12.4	long-axis asymmetric slide
	3	130	0.005	1398	−0.12	−9.9	ring breathing/C-C-H bending
	4	115	0.012	1236	−0.10	−8.5	C-C-H bending
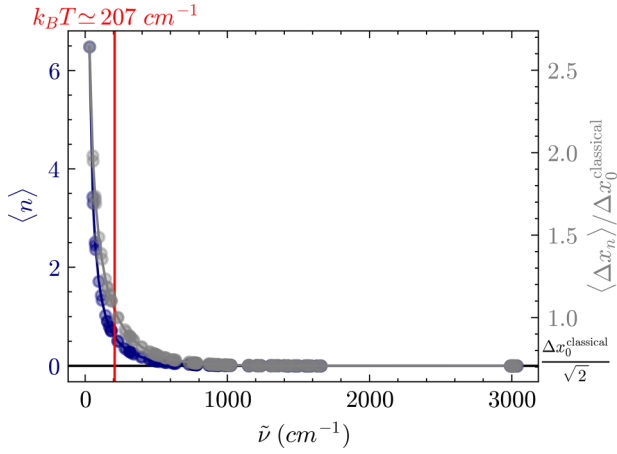
FIG. 7. Expected vibrational quantum number ($\langle n \rangle$, dark blue) and the uncertainty (Δx_n, gray) in the position at 300 K as a fraction of the zero-point energy level maximum classical displacement amplitude ($\Delta x_0^{\text{classical}}$) for each normal mode.

APPENDIX A: PREDICTING CHARGE-CARRIER MOBILITIES WITH BOLTZMANN TRANSPORT THEORY

Anisotropic charge-carrier mobilities [$\mu_{\alpha\beta}$, Eq. (A1)] can be extracted from periodic density-functional-theory-derived electrical conductivities [σ, Eq. (A2)] and charge-carrier concentrations within the constant relaxation time Boltzmann transport theory approximation,

$$\mu_{\alpha\beta} = \frac{\sigma_{\alpha\beta}V}{eN_{\mathcal{F},T}}, \qquad (A1)$$

$$\sigma_{\alpha\beta}(\mathcal{F},T) = e^2 \int dE \left(-\frac{\partial f_0(E,T)}{\partial E} \right) \Xi_{\alpha\beta}(E). \qquad (A2)$$

Here, $\mu_{\alpha\beta}$ is the charge-carrier mobility [Eq. (A1)] matrix element in the $\alpha\beta$ direction of the cell. $\mathcal{F}$ is the approximate Fermi level from the highest-energy k point at the top of the valence bands, E is the energy, V is the volume of the
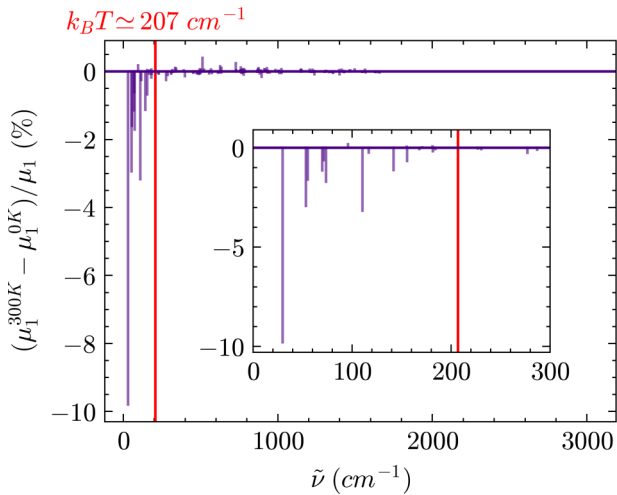

FIG. 8. Differences in the normal-mode-induced mobility between 300 and 0 K as a percent of mobility along the primary axis in the optimized structure (μ_1). The red vertical line marks room temperature (300 K).
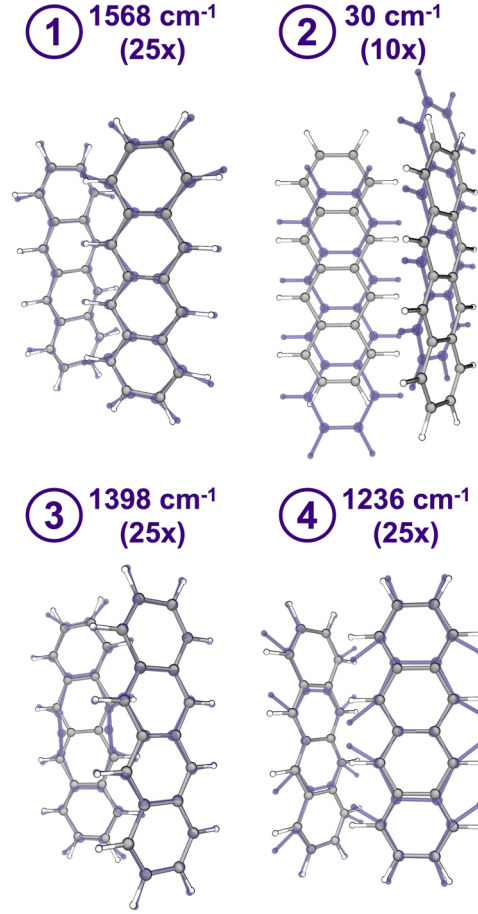

FIG. 9. Dimers depicting the four most detrimental modes at 300 K. Gray/white show the optimized structures and the finite-displaced structure of each mode is shown as a multiple (10x or 25x) of the maximum classical displacement (dark purple).

primitive unit cell, and e is the fundamental charge of the carrier. $N_{\mathcal{F},T}$ is the DFT-derived number of charge carriers at a particular energy,

$$N_{F,T} = \frac{n}{N_{\mathbf{k}}} \sum_{\mathbf{k}} \sum_{i} \frac{1}{\exp\left(\frac{E-\mathcal{F}}{k_B T}\right) + 1} \Theta[E - E_i(\mathbf{k})], \qquad (A3)$$

where n is the number of electrons per state, $N_{\mathbf{k}}$ is the number of k points, and $\Theta[E - E_i(\mathbf{k})]$ is the theta function. The conductivity $\sigma_{\alpha\beta}$ is a symmetric second-rank 3×3 tensor with nine unique coefficients [Eq. (A4)],

$$[\sigma] = \begin{bmatrix} \sigma_{\alpha\alpha} & \sigma_{\alpha\beta} & \sigma_{\alpha\gamma} \\ \sigma_{\beta\alpha} & \sigma_{\beta\beta} & \sigma_{\beta\gamma} \\ \sigma_{\gamma\alpha} & \sigma_{\gamma\beta} & \sigma_{\gamma\gamma} \end{bmatrix}. \qquad (A4)$$

In BTE, σ is derived from the integral over the energy of the product of the negative partial derivative of the Fermi Dirac distribution with respect to energy ($\partial f_0/\partial E$). The transport distribution function [χ, Eq. (A5)] is the product of the band velocities [$v_{i,\alpha}(\boldsymbol{K}) = \partial E_i(\boldsymbol{K})/\partial k_\alpha$] indexed over each band combination, i and j,

$$\Xi_{\alpha\beta}(E) = \tau \sum_{\boldsymbol{K}} \frac{1}{N_K V} \sum_{i,j} v_{i,\alpha}(\boldsymbol{K}) v_{j,\beta}(\boldsymbol{K}). \qquad (A5)$$
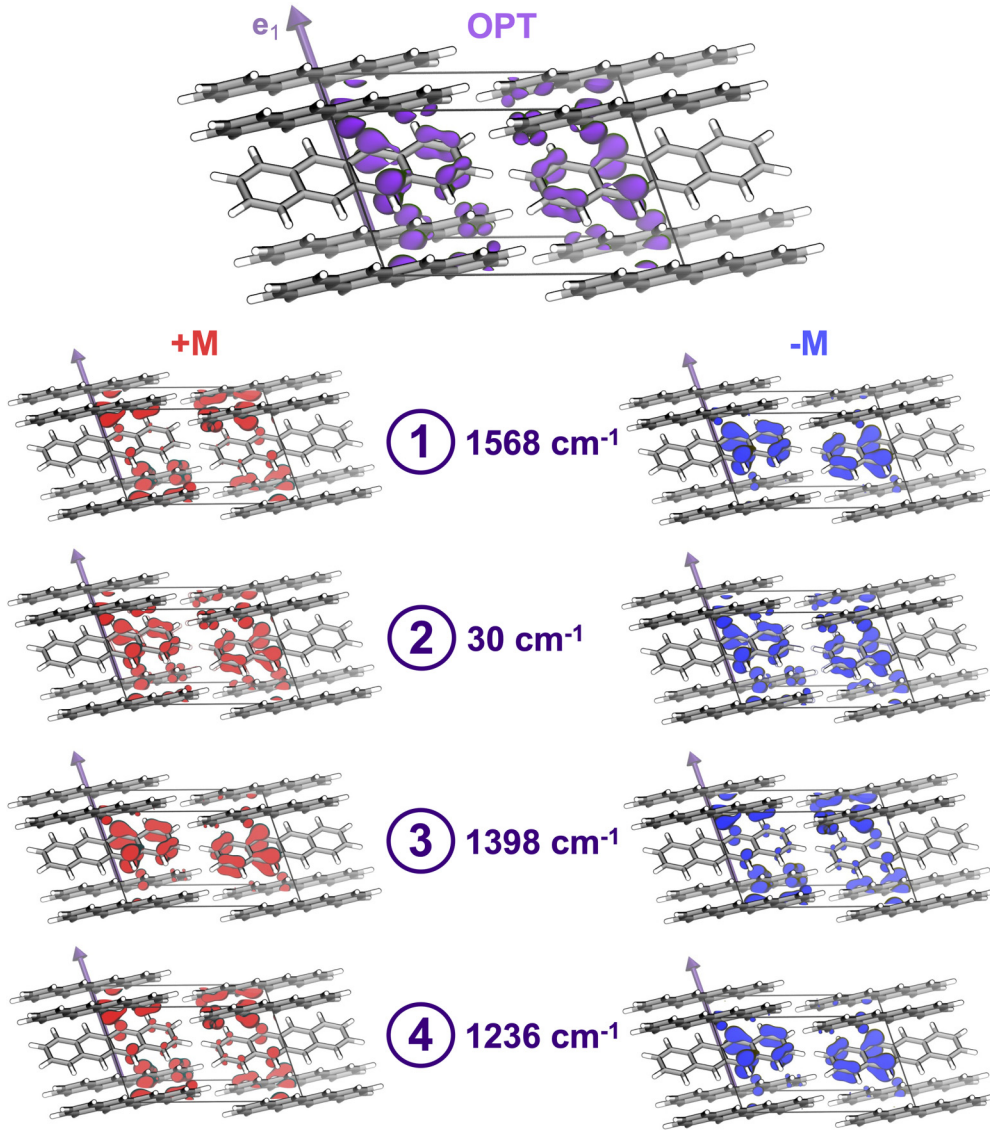
FIG. 10. Effect of finite displacement on the valence band (VB) projected density. The optimized VB is plotted in purple, while the density resulting from $+\mathbf{M}$ (red) and $-\mathbf{M}$ (blue) finite displacement is shown for the four worst modes at 300 K. The VB projected density matrices are plotted as an isosurface with an isovalue of 0.03.

In the constant relaxation time approximation, Ξ includes a time τ that approximates the mean charge-carrier lifetime. Through the paper, τ is assumed to be 2 fs to match what has been predicted for similar organic materials [52,53].

APPENDIX B: DETERMINING THE PRINCIPAL TRANSPORT AXES FROM BTE CALCULATIONS

For isotropic conductors, Ohm's law is defined as $\mathbf{J} = \sigma \mathbf{E}$, where σ is the conductivity, $\mathbf{E}$ is the direction of the applied electric field and $\mathbf{J}$ is the current from the applied field. As the current is not necessarily parallel to the applied field, the anisotropic form of Ohm's law is

$$J_\alpha = \sigma_{\alpha\beta} E_\beta. \tag{B1}$$

With this, the electrical current can be determined from an applied field with a set of arbitrary defined Cartesian basis vectors, x, y, and z. The current density vector depends on all of the electric field components simultaneously,

$$j_x = \sigma_{xx} E_x + \sigma_{xy} E_y + \sigma_{xz} E_z, \tag{B2}$$

$$j_y = \sigma_{yx} E_x + \sigma_{yy} E_y + \sigma_{yz} E_z, \tag{B3}$$

$$j_z = \sigma_{zx} E_x + \sigma_{zy} E_y + \sigma_{zz} E_z. \tag{B4}$$

This makes the electrical conductivity a second-rank 3×3 tensor with the number of coefficients depending on the symmetry of the crystal. For higher symmetry crystals, the off-diagonal terms may vanish and the diagonal terms can even become equivalent.

With the symmetric second-rank 3×3 conductivity tensor, i.e., $\sigma_{\alpha\beta} = \sigma_{\beta\alpha}$, it is possible to transform the arbitrary basis

vectors into a set of principal axes to simplify the current vectors to

$$j_1 = \sigma_{11}E_1, \tag{B5}$$

$$j_2 = \sigma_{22}E_2, \tag{B6}$$

$$j_3 = \sigma_{33}E_3, \tag{B7}$$

where $\sigma_{11}, \sigma_{22}, \sigma_{33} \equiv \sigma_1, \sigma_2, \sigma_3$. To do this, the tensor is diagonalized to satisfy the secular equation, $|\sigma - \lambda \mathbf{I}| = 0$. The resulting eigenvalues, or principal values, that satisfy the equation are labeled in the text as σ_1, σ_2, and σ_3.

APPENDIX C: FINITE NORMAL-MODE DISPLACEMENTS OF UNIT CELLS

In periodic crystalline systems, the temperature-dependent dynamic structural disorder can be simply and efficiently described by the normal-mode basis at the Γ point of a particular crystal. The inclusion of phonon dispersion beyond the Γ point is important, but the cost of evaluating such effects often prohibits it in practice [61]. Recent evaluation of the full Brillouin zone shows that Γ-point analyses can underestimate the effect of dynamic disorder [39]. At the Γ point of a crystal, the total number of normal modes is determined by the number of spatial dimensions multiplied by the number of atoms in the primitive/unit/super cell, minus the three zero-energy translational modes ($3N - 3$). Each normal mode, represented by i, has a quantized energy (eigenvalue, $\hbar\omega_i$) and an eigenvector

(a displacement matrix, $+/-\mathbf{M}$) that describes how each atom of the cell moves as a function of time. In this study, the harmonic approximation was used to displace the atoms in either positive ($+\mathbf{M}$) or negative ($-\mathbf{M}$) directions. In either direction, the energies are assumed to be equivalent for small displacement amplitudes. The matrix elements of the Hessian (i.e., the second derivatives of the energy) were determined numerically with the analytical gradients. Frequencies were determined by diagonalizing the mass-weighted Hessian. The resulting eigenvectors are the normal modes [43,44].

The displacement amplitudes of each normal modes are determined from the uncertainty in the positions from the operator $\Delta\hat{x}_n$. The displacements are correlated to temperature according to

$$\Delta\hat{x}_n = \Delta\hat{x}_0\sqrt{(2n+1)}$$
$$= \sqrt{\left(\frac{\hbar}{2m\omega}\right)\left(\frac{2}{e^{\hbar\omega/k_BT} - 1} + 1\right)}. \tag{C1}$$

In this expression, $\Delta\hat{x}_0$ is the uncertainty in the positions at the zero-point energy level, n is the Bose-Einstein occupation number, T is the temperature, ω is the normal-mode frequency, m is the reduced mass of the normal mode, $\hbar$ is the reduced Planck's constant, and k_B is Boltzmann's constant. The conductivity and mobility changes for each normal mode can be evaluated at the extrema of the uncertainty displacements at any finite temperature. In the limit where $n = 0$, the displacements are equivalent to a quantum mechanical zero-point energy asymptote.

---

[1] L. Jiang, H. Dong, and W. Hu, J. Mater. Chem. **20**, 4994 (2010).

[2] K. Liu, B. Ouyang, X. Guo, Y. Guo, and Y. Liu, npj Flex. Electron. **6**, 1 (2022).

[3] J. Bauri, R. B. Choudhary, and G. Mandal, J. Mater. Sci. **56**, 18837 (2021).

[4] L. X. Chen, ACS Energy Lett. **4**, 2537 (2019).

[5] M. Imran and M. S. Chen, ACS Appl. Mater. Interfaces **14**, 1817 (2022).

[6] V. Coropceanu, J. Cornil, D. A. da Silva Filho, Y. Olivier, R. Silbey, and J. L. Brédas, Chem. Rev. **107**, 926 (2007).

[7] A. Troisi and G. Orlandi, J. Phys. Chem. A **110**, 4065 (2006).

[8] Y. Diao, K. M. Lenn, W. Y. Lee, M. A. Blood-Forsythe, J. Xu, Y. Mao, Y. Kim, J. A. Reinspach, S. Park, A. Aspuru-Guzik, G. Xue, P. Clancy, Z. Bao, and S. C. Mannsfeld, J. Am. Chem. Soc. **136**, 17046 (2014).

[9] B. B. Patel and Y. Diao, Nanotechnology **29**, 044004 (2018).

[10] X. Yu, V. Kalihari, C. D. Frisbie, N. K. Oh, and J. A. Rogers, Appl. Phys. Lett. **90**, 162106 (2007).

[11] A. Troisi, Chem. Soc. Rev. **40**, 2347 (2011).

[12] F. Ortmann, F. Bechstedt, and K. Hannewald, Phys. Stat. Sol. B **248**, 511 (2011).

[13] V. Coropceanu, Y. Li, Y. Yi, L. Zhu, and J. L. Brédas, MRS Bull. **38**, 57 (2013).

[14] A. Girlando, L. Grisanti, M. Masino, I. Bilotti, A. Brillante, R. G. Della Valle, and E. Venuti, Phys. Rev. B **82**, 035208 (2010).

[15] A. S. Eggeman, S. Illig, A. Troisi, H. Sirringhaus, and P. A. Midgley, Nat. Mater. **12**, 1045 (2013).

[16] S. Fratini, D. Mayou, and S. Ciuchi, Adv. Funct. Mater. **26**, 2292 (2016).

[17] S. Illig, A. S. Eggeman, A. Troisi, L. Jiang, C. Warwick, M. Nikolka, G. Schweicher, S. G. Yeates, Y. Henri Geerts, J. E. Anthony, and H. Sirringhaus, Nat. Commun. **7**, 10736 (2016).

[18] S. Fratini, S. Ciuchi, D. Mayou, G. T. De Laissardière, and A. Troisi, Nat. Mater. **16**, 998 (2017).

[19] W. Li, J. Ren, and Z. Shuai, Nat. Commun. **12**, 4260 (2021).

[20] T. Nematiaram, S. Ciuchi, X. Xie, S. Fratini, and A. Troisi, J. Phys. Chem. C **123**, 6989 (2019).

[21] A. Landi, J. Phys. Chem. C **123**, 18804 (2019).

[22] E. G. Bittle, A. J. Biacchi, L. A. Fredin, A. A. Herzing, T. C. Allison, A. R. Hight Walker, and D. J. Gundlach, Commun. Phys. **2**, 29 (2019).

[23] G. Schweicher, G. D'Avino, M. T. Ruggiero, D. J. Harkin, K. Broch, D. Venkateshvaran, G. Liu, A. Richard, C. Ruzié, J. Armstrong, A. R. Kennedy, K. Shankland, K. Takimiya, Y. H. Geerts, J. A. Zeitler, S. Fratini, and H. Sirringhaus, Adv. Mater. **31**, 1902407 (2019).

[24] S. Fratini, M. Nikolka, A. Salleo, G. Schweicher, and H. Sirringhaus, Nat. Mater. **19**, 491 (2020).

[25] S. Giannini, O. G. Ziogos, A. Carof, M. Ellis, and J. Blumberger, Adv. Theor. Simul. **3**, 2000093 (2020).

[26] S. Giannini and J. Blumberger, Acc. Chem. Res. **55**, 819 (2022).

[27] W. Q. Deng and W. A. Goddard, J. Phys. Chem. B **108**, 8614 (2004).

[28] A. Troisi and G. Orlandi, J. Phys. Chem. B **109**, 1849 (2005).

[29] E. F. Valeev, V. Coropceanu, D. A. Da Silva Filho, S. Salman, and J. L. Brédas, J. Am. Chem. Soc. **128**, 9882 (2006).

[30] N.-E. Lee, J.-J. Zhou, L. A. Agapito, and M. Bernardi, Phys. Rev. B **97**, 115203 (2018).

[31] Z. J. Knepp and L. A. Fredin, J. Phys. Chem. A **126**, 3265 (2022).

[32] Z. J. Knepp, G. B. Masso, and L. A. Fredin, J. Chem. Phys. **158**, 064704 (2023).

[33] A. Landi, R. Borrelli, A. Capobianco, A. Velardo, and A. Peluso, J. Chem. Theory Comput. **14**, 1594 (2018).

[34] Y. Jiang, H. Geng, W. Li, and Z. Shuai, J. Chem. Theory Comput. **15**, 1477 (2019).

[35] S. Fratini and S. Ciuchi, Phys. Rev. Res. **2**, 013001 (2020).

[36] T. Otaki, T. Terashige, J. Tsurumi, T. Miyamoto, N. Kida, S. Watanabe, T. Okamoto, J. Takeya, and H. Okamoto, Phys. Rev. B **102**, 245201 (2020).

[37] P. A. Banks, A. M. Dyer, A. C. Whalley, and M. T. Ruggiero, Chem. Commun. **58**, 12803 (2022).

[38] P. A. Banks, G. D'Avino, G. Schweicher, J. Armstrong, C. Ruzié, J. W. Chung, J. I. Park, C. Sawabe, T. Okamoto, J. Takeya, H. Sirringhaus, and M. T. Ruggiero, Adv. Funct. Mater. **33**, 2303701 (2023).

[39] D. Vong, T. Nematiaram, M. A. Dettmann, T. L. Murrey, L. S. R. Cavalcante, S. M. Gurses, D. Radhakrishnan, L. L. Daemen, J. E. Anthony, K. J. Koski, C. X. Kronawitter, A. Troisi, and A. J. Moulé, J. Phys. Chem. Lett. **13**, 5530 (2022).

[40] T. F. Harrelson, V. Dantanarayana, X. Xie, C. Koshnick, D. Nai, R. Fair, S. A. Nuñez, A. K. Thomas, T. L. Murrey, M. A. Hickner, J. K. Grey, J. E. Anthony, E. D. Gomez, A. Troisi, R. Faller, and A. J. Moulé, Mater. Horiz. **6**, 182 (2019).

[41] M. A. Dettmann, L. S. R. Cavalcante, C. A. Magdaleno, and A. J. Moulé, Adv. Funct. Mater. **33**, 2213370 (2023).

[42] R. B. Campbell, J. M. Robertson, and J. Trotter, Acta Crystallogr. **15**, 289 (1962).

[43] R. Dovesi, A. Erba, R. Orlando, C. M. Zicovich-Wilson, B. Civalleri, L. Maschio, M. Rérat, S. Casassa, J. Baima, S. Salustro, and B. Kirtman, WIREs Comput. Mol. Sci. **8**, e1360 (2018).

[44] R. Dovesi, F. Pascale, B. Civalleri, K. Doll, N. M. Harrison, I. Bush, P. D'Arco, Y. Noel, M. Rera, P. Carbonniere, M. Causa, S. Salustro, V. Lacivita, B. Kirtman, A. M. Ferrari, F. S. Gentile, J. Baima, M. Ferrero, R. Demichelis, and M. De La Pierre, J. Chem. Phys. **152**, 204111 (2020).

[45] L. Doná, J. G. Brandenburg, and B. Civalleri, J. Chem. Phys. **151**, 121101 (2019).

[46] S. Grimme, J. Antony, S. Ehrlich, and H. Krieg, J. Chem. Phys. **132**, 154104 (2010).

[47] J. C. Costa, R. J. Taveira, C. F. Lima, A. Mendes, and L. M. Santos, Opt. Mater. **58**, 51 (2016).

[48] H. Morisaki, T. Koretsune, C. Hotta, J. Takeya, T. Kimura, and Y. Wakabayashi, Nat. Commun. **5**, 5400 (2014).

[49] A. Vollmer, R. Ovsyannikov, M. Gorgoi, S. Krause, M. Oehzelt, A. Lindblad, N. Mårtensson, S. Svensson, P. Karlsson, M. Lundvuist, T. Schmeiler, J. Pflaum, and N. Koch, J. Electron Spectrosc. Relat. Phenom. **185**, 55 (2012).

[50] G. Sansone, A. Ferretti, and L. Maschio, J. Chem. Phys. **147**, 114101 (2017).

[51] J. Linnera, G. Sansone, L. Maschio, and A. J. Karttunen, J. Phys. Chem. C **122**, 15180 (2018).

[52] Y. C. Cheng, R. J. Silbey, D. A. Da Silva Filho, J. P. Calbert, J. Cornil, and J. L. Brédas, J. Chem. Phys. **118**, 3764 (2003).

[53] M. J. Schilcher, P. J. Robinson, D. J. Abramovitch, L. Z. Tan, A. M. Rappe, D. R. Reichman, and D. A. Egger, ACS Energy Lett. **6**, 2162 (2021).

[54] C. Reese, W. J. Chung, M. M. Ling, M. Roberts, and Z. Bao, Appl. Phys. Lett. **89**, 202108 (2006).

[55] K. Hannewald, V. M. Stojanović, and P. A. Bobbert, J. Phys.: Condens. Matter **16**, 2023 (2004).

[56] S.-h. Wen, A. Li, J. Song, W.-q. Deng, K.-l. Han, and W. A. Goddard, J. Phys. Chem. B **113**, 8813 (2009).

[57] N. Koch, A. Vollmer, I. Salzmann, B. Nickel, H. Weiss, and J. P. Rabe, Phys. Rev. Lett. **96**, 156803 (2006).

[58] R. C. Hatch, D. L. Huber, and H. Höchst, Phys. Rev. Lett. **104**, 047601 (2010).

[59] Y. Li, V. Coropceanu, and J. L. Brédas, J. Phys. Chem. Lett. **3**, 3325 (2012).

[60] L. Graf, A. Kusber, B. Büchner, and M. Knupfer, Phys. Rev. B **106**, 165429 (2022).

[61] Z. Tu, Y. Yi, V. Coropceanu, and J.-L. Brédas, J. Phys. Chem. C **122**, 44 (2018).